Quantifying the impact of electric fields on the local structure and migration of potassium ions at the orthoclase (001) surface

Michel Sassi[1]*, Sebastien N. Kerisit[1], Pauline G. Simonnin[1], Benjamin A. Legg[1], Elias Nakouzi[1], Yue Zhu[2], Timothy C. Johnson[2], Kevin M. Rosso[1]

[1]Physical and Computational Sciences Directorate, Pacific Northwest National Laboratory, Richland, WA 99352, USA.

[2]Energy and Environment Directorate, Pacific Northwest National Laboratory, Richland, WA 99352, USA.

Abstract

Developing an understanding of the response of mineral/water interfaces to applied electric fields is central to detecting and interpreting signatures of interfacial processes in the subsurface. Here we focus density functional theory calculations on understanding K^+ cation binding and migration across the (001) surface of orthoclase feldspar under various applied electric fields with and without surface hydration. The calculations reveal how water ligands labilize surface K^+ cations for migration while also increasing their sensitivity to electric field effects on the binding energy at different surface sites. The calculations also show how the direction and strength of the electric field systematically affect surface cation mobility, sorption, and hydration behavior. Specifically, electric fields directed toward the surface reduce the energy gap between the different surface potassium sites, favor hydration, and shorten K^+ residence time at their crystallographic site. The findings help fill a major knowledge gap into the impact of electric fields on mineral/water interface structure and dynamics more generally, featuring in this case a commonly found type of feldspar involved in a multitude of atmospheric and geochemical processes.

Introduction

The organization and dynamics of ions at mineral/water interfaces control many reactions in natural and industrial systems. Depending on the pH and composition of the aqueous solution, most mineral surfaces will bear a net electrical charge due to specific ion adsorption, which is subsequently neutralized by a diffuse swarm of surrounding counterions. Stern layer ions making up the near-surface region are generally located within the first two water monolayers (~6 Å), whereas the diffuse layer lies beyond.[1,2] This electrical double-layer (EDL) concept provides a useful framework for understanding interfacial properties that impact reactivity, such as the adsorption capacity, redox potential, and interparticle forces that cause them to aggregate/disaggregate.[3-5] EDL properties thus play an important role in a variety of contexts including catalysis,[6] cement corrosion,[7] aquatic geochemistry,[8,9] and the transport of metals in soil and sedimentary rocks.[10,11]

However, current EDL models provide only a limited picture of the interface that focuses on a static one-dimensional treatment of net charge distribution averages along the surface normal direction at equilibrium. In reality, interfacial ion distributions are based on a dynamical equilibrium, one that is readily perturbed when gradients in chemical and/or electrostatic potential that drive reactions exist. Hence, ion mobilities become an important part of understanding interfacial reactions, requiring more detailed knowledge of ion-ion, ion-surface, and ion-solvent interactions that control ion dynamics in the EDL in three dimensions. Ion dynamics is particularly important under conditions of applied electric field, where current EDL models have questionable value for explaining electrokinetic phenomena.[12]

This deficit continues to propagate into a relatively poor understanding of electrical signatures of mineral/water interfaces, such as those detected using electrical impedance spectroscopy (EIS). One form of EIS ongoing development for field-scale sensing is called spectral induced polarization (SIP). SIP is a promising method to remotely interrogate physicochemical processes occurring in subsurface environments based on measurements of the frequency-dependent polarization response.[13-16] Surface reactions like oxidation-reduction or the precipitation-adsorption of secondary minerals phases such as Fe(III)-oxyhydroxide that lead to changes in the electrical properties can be detected by analyzing SIP responses.[17,18] Unfortunately, not enough is yet known about the dynamics of EDL ion polarization and relaxation to interpret SIP signals unambiguously.

Computational molecular simulations have begun to provide insight into electric field effects on EDL ions at mineral/water interfaces. Simulations based on classical force field molecular dynamics (MD) have proven especially valuable given their ability to efficiently model water and ion dynamics at nanometer scales under applied electric fields, including for quartz,[19,20] clays,[21] and feldspar surfaces.[22,23] However, these simulations typically rely on less expensive non-polarizable, non-reactive force fields to build a response to applied electric fields. They furthermore cannot account for the electronic structure at the mineral/water interface. In these regards, first-principles density functional theory (DFT) methods are desirable for their

improved accuracy, albeit at the expense of much more restricted length and time scales that can be addressed. Although DFT methods have been used to quantify the impact of electric fields on physical and chemical processes such as magnetic phase transitions,[24] catalytic water dehydrogenation,[25] and surface diffusion,[26] to the best of our knowledge this approach has yet to be explicitly directed at improving the fundamental basis for interpreting EIS/SIP observables. Because of its computational expense, however, DFT ultimately needs to be coupled to larger-scale MD simulations for a more comprehensive treatment.

Here we report a DFT-based modeling study of electric field effects on potassium cation (K^+) diffusion dynamics along vacuum and hydrated surfaces of the common potassium feldspar mineral orthoclase ($KAlSi_3O_8$). By focusing exclusively on the Stern layer, this work is complementary to recent molecular dynamics simulations performed by Kerisit *et al.*[23] in which field-driven ion mobilities at the stable orthoclase (001) facet in contact with a 1 M NaCl aqueous solution were examined. While the faster mobilities of fully hydrated outer-sphere Na^+/K^+ ions is more consistent with those that would typify cations in the diffuse layer, the slower process of field-driven displacement and diffusion of partially hydrated Stern layer cations along the surface was not specifically addressed, despite its potential importance to storage of electrical polarization energy and the subsequent relaxation response of the EDL when the field is removed. The present study therefore specifically investigates electric field effects on the surface charge density distribution and likewise the energy barriers for Stern layer K^+ cations to migrate via various possible exposed lattice sites. We examine two interface systems, orthoclase (001)/vacuum and orthoclase (001)/water, to evaluate the impact of hydration on K^+ surface migration.

The calculations revealed that water facilitates the migration of surface K^+ while increasing the sensitivity of different surface potassium sites to applied electric fields. In addition, the direction of the electric field was found to affect the diffusion, sorption, and hydration behavior of surface K^+ profoundly. While the strength of the electric field applied in this work (~10^9 V/m) is much larger than what can typically be found in natural conditions (~100 V/m),[27] it is relevant at the nanometer scale where, for example, a highly localized and directional electric field can be applied between a STM tip and a substrate.[28] Our findings provide quantitative information and atomistic-level insights of the impact of electric fields at mineral/water interfaces for a commonly found type of feldspar, particularly at non-equilibrium local electrostatic conditions arising from applied fields akin to those used in electrochemical sensing measurements.[29-34]

Computational Methods

Density functional theory (DFT) simulations were carried out using VASP (Vienna ab initio simulation package).[35-38] The exchange-correlation functional used the generalized gradient

approximation (GGA), as parametrized by Perdew-Burke-Ernzerhof (PBE),[39] and the Grimme[40] dispersion corrections (i.e., PBE+D3). All the calculations accounted for spin-polarization and used a cutoff energy of 520 eV.

The relaxation of bulk orthoclase mineral, shown in Figure 1a, used a 1×1×2 supercell translation of the primitive cell. The orthoclase crystal structure has two tetrahedral sites referred to as T1 and T2 sites. The orthoclase supercell used the Si and Al occupations determined by Kimata *et al.*[41] from single-crystal X-ray diffraction refinement (Al mole fractions of 0.325 and 0.148 for T1 and T2 sites, respectively) and implemented in previous atomistic models.[42-45] The convergence criterion for the total energy was 10^{-5} eV/cell and 10^{-4} eV/Å for the force components. A Monkhorst-Pack[46] *k*-point mesh sampling of 8×6×6 was used, and the relaxed lattice parameters were *a*=8.631 Å (+0.67%), *b*=13.099 Å (+0.71%), *c*=7.244 Å (+0.74%), and β=116.05° (-0.02%), which are in good agreement with the experimental values of *a*=8.574 Å, *b*=13.006 Å, *c*=7.191 Å, and β=116.07°.[41]

To model the orthoclase (001) surface, a stoichiometric, symmetric, charge neutral, and hydroxylated bilayer slab model was created in an orthorhombic periodic box of size 17.262 Å × 13.099 Å × 34.0 Å, as shown in Figure 1b. The Monkhorst-Pack *k*-point mesh sampling used for surface calculations was 4×6×1. In all the simulations using a slab model, only the top layer atoms were allowed to relax, while the bottom layer atoms, highlighted by the grey area in Figure 1b, were kept in their relaxed bulk positions. Periodic images of the orthoclase slab were separated by a vacuum space of at least 19 Å. A top view of the orthoclase (001) surface, shown in Figure 1c, highlights the two surface sites, labelled #1 and #2, that were investigated in this study as sites K^+ ions would hop to, from their crystallographic site, to diffuse on the surface. The non-crystallographic #1 and #2 surface K^+ sites are still located in a cavity formed by eight Al/Si tetrahedra and were chosen based on the local geometry of the cavity. Two systems were considered in this work, an orthoclase (001)/vacuum and orthoclase (001)/water interface. The latter was obtained by adsorbing one monolayer (1 ML) of water molecules on the orthoclase (001) surface. The initial positions of the water molecules were extracted from a previous MD simulation.[42] The structure of the hydrated slab model used is provided in supplementary information.

To explore the effects of electric fields on the surface structure and potassium migration, a uniform electric field, E, was applied perpendicular to the slab surface in directions pointing either toward the surface (i.e., $E < 0$) or away from it (i.e., $E > 0$). The electric field intensity was limited to ± 0.3 eV/Å. As previously noted,[25,26,47] care is needed to perform simulations with electric fields. In VASP, external electric fields are applied following the approach of Neugebauer and Scheffler, in which an artificial dipole sheet is introduced in the middle of the vacuum space.[48] This method requires enough vacuum space to prevent the artificial dipole sheet and the charge density of the slab from overlapping.[26] In our systems, the separation distance between the

surface and the dipole sheet was about 9.5 Å and the work function was 6.16 eV. This suggests that the charge density decays by 1 order of magnitude every 0.87 Å and is thus negligible at the location of the dipole sheet. However, when the vacuum size is too large, electrons at the Fermi level of the surface can tunnel to the vacuum resulting in field emissions.[25,26] To avoid electron tunneling, the distance between the surface and the dipole sheet should not exceed $\frac{\Phi}{E}$ where Φ is the work function (6.16 eV) and E is the electric field ($\leq$0.3 eV/Å), yielding a maximal distance of about 20.53 Å.

The energy barriers along the migration path of surface K^+ and the Bader charges of the species were calculated, respectively, using the climbing image nudged elastic band (CI-NEB) method[49] with the Quick-Min algorithm and default parameters, and the Bader code,[50-53] both available from the VASP transition state theory (VTST) website.[54]

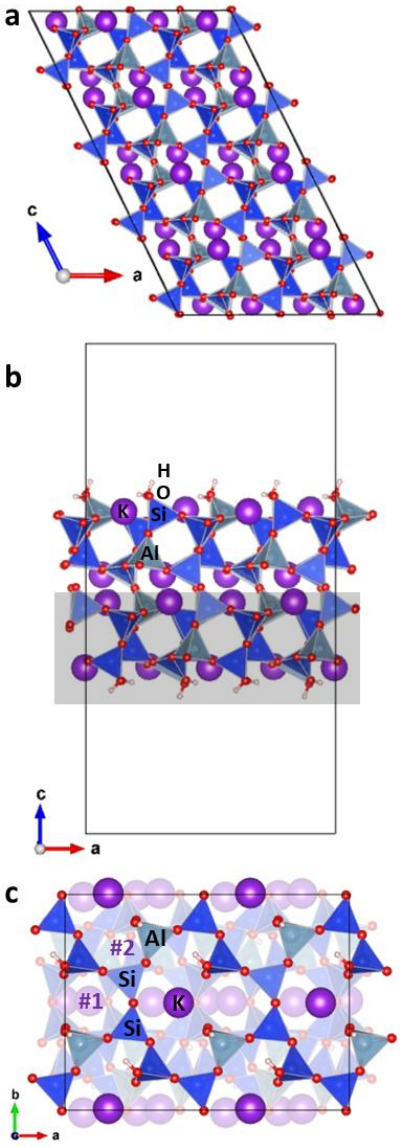

Figure 1: (a) Orthoclase crystal structure. (b) Lateral view of the slab used to model a hydroxylated orthoclase (001) surface. The greyed area shows the atoms that were kept fixed in a bulk-like configuration. (c) Top view of the orthoclase (001) surface. Purple, dark blue, light blue, red, and pink spheres represent K, Si, Al, O, and H species, respectively.

Results and Discussion

Effect of electric fields on electron density and charge. Two systems were considered to quantify the effects of electric fields and the presence of water on the electronic structure of the orthoclase (001) surface and the dynamics of K^+ surface migration. The first system is an orthoclase (001)/vacuum interface, shown in Figure 2a, and the second system is an orthoclase (001)/water interface, shown in Figure 2b, in which the orthoclase surface is in contact with 1

monolayer (ML) of water molecules. For each system, Figure 2 shows the electron density difference at constant potential calculated for an electric field intensity of 0.1 eV/Å and 0.3 eV/Å normal to the surface. Stronger redistributions of the electronic density around atoms are obtained for electric fields with higher intensities.

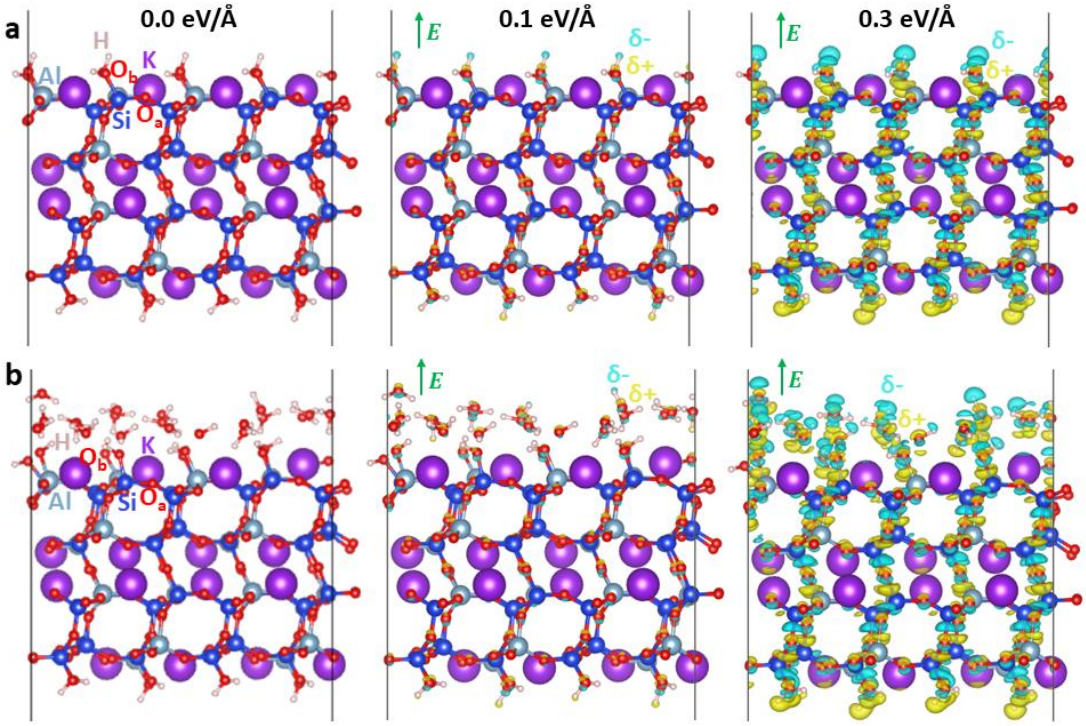

Figure 2: Electron density differences at the orthoclase (001) surface in (a) vacuum and (b) in contact with 1 ML of water, calculated for different electric field intensities normal to the surface. The electronic changes are shown for an iso-density value of 2.7×10^{-3} e-/Å^3. The gain and loss of electrons is respectively symbolized by cyan (δ-) and yellow (δ+) iso-surfaces. The direction of the electric field, E (>0), is indicated by the green arrow.

In addition to the 3D electron density difference plots, the Bader charges of surface species were calculated as function of electric field intensity. Table 1 lists the average Bader charges for both interface systems for electric fields oriented upward or downward along the surface normal direction. In Table 1, the labels O_a and O_b refer to oxygen atoms bonded to Al or Si atoms, and to protons (hydroxyl oxygens), respectively (Figure 2). A negligible variation of the Bader charges is obtained for each species (Table 1), indicating that the atomic charges are not sensitive to the electric field intensity. Overall, the electron density difference plots and the negligible variation of the Bader charges indicate that electric fields polarize the electronic clouds

of the atoms, thereby inducing bond polarization, without inducing charge transfer between atoms.

Electric field magnitude in (eV/Å)	**0.0**	**|0.1|**	**|0.3|**
Species	*Orthoclase (001)/Vacuum*		
K	0.89	0.89	0.90
Al	2.44	2.44	2.44
Si	3.15	3.15	3.14
O_a	-1.60	-1.60	-1.60
O_b	-1.45	-1.44	-1.43
H	0.65	0.64	0.63
Species	*Orthoclase (001)/Water*		
K	0.89	0.89	0.89
Al	2.44	2.44	2.45
Si	3.15	3.15	3.16
O_a	-1.60	-1.60	-1.60
O_b	-1.46	-1.46	-1.47
H	0.66	0.66	0.65

Table 1: Average Bader charges (in e^-) as function of the electric field intensity for the species at the orthoclase (001) surface in vacuum and in contact with 1 ML of water. The species labels are shown in Figure 2.

Effect of electric fields on the relative energy of surface K^+ sites. Next, we characterize the impact of electric fields, with and without water present, on the relative energetics of three surface potassium sites: its crystallographic surface site and two neighboring surface sites labeled site #1 and #2 in Figure 1c. The most stable surface site for K^+ is its crystallographic site (Figure 1c) across the full range of electric field intensities investigated (i.e., from -0.3 eV/Å to 0.3 eV/Å) and for both systems. Therefore, the energies of sites #1 and #2 are reported relative to the energy of the crystallographic surface site (Figure 3a and 3b). The relative energies at each value of the electric field were calculated for both an unrelaxed interface and for a geometry-optimized interface (Figure 3a and 3b). In the former case, the system was first optimized without an applied electric field and then kept fixed when the electric field was applied. In the case of the orthoclase (001)/vacuum interface (Figure 3a), the structural optimization of the surface yields a slightly lower energy than that of the unrelaxed surface and this energy gain increases as the absolute value of the applied electric field increases. This result indicates that an applied electric field induces structural relaxation of the orthoclase (001)/vacuum interface. However, in the case of the orthoclase (001)/water interface (Figure 3b), the effect of structural relaxation on the relative

energies of sites #1 and #2 is much less noticeable as the relative energies of the unrelaxed and optimized interface systems are almost identical across the range of electric field intensities investigated. For both cases, details of the structural relaxations involved will be discussed later.

While a potassium cation located in its native crystallographic surface site is the most energetically favorable position, Figure 3 also shows that for both interface systems, orthoclase (001)/vacuum and orthoclase (001)/water, having a potassium in site #2 is less energetically favorable than in site #1. This is in part due to fewer K—O contacts with orthoclase surface, as shown in Figure 3c. To understand the role of hydration on K^+ ion binding in various positions on the surface, Figure 3c shows the coordination shell of surface K^+ ions at the crystallographic site, site #1, and site #2 when 1 ML of water is present at the interface but at zero applied electric field. In the crystallographic site, site #1, and site #2, K^+ ions adopt a partially hydrated inner-sphere complex and are respectively coordinated with 6, 7, and 4 oxygen atoms when 1 ML of hydration is available. In the crystallographic site K^+ is bonded to only two water molecules with bond lengths of 2.92 Å and 2.83 Å, and is also in contact with 3 surface O atoms with bond lengths ranging from 2.93 Å to 3.0 Å. At sites #1 and #2, K^+ is bonded to three water molecules with shorter bond lengths (2.73-2.88 Å) in the case of site #1 than for site #2 (2.90-2.97 Å). Hence the availability of hydration water can be expected to play an important role in ameliorating differences in site binding energetics.

Interestingly, an electric field directed toward the surface (i.e., $E < 0$) tends to reduce the energy gap between all sites, that is, sites #1, #2, and the crystallographic site, while an electric field directed away from the surface (i.e., $E > 0$) tends to increase the energy gap between all sites. This suggests that for a strong enough electric field directed toward the surface, all the surface potassium sites of orthoclase (001) would ultimately be of similar energy. While most of the calculated data sets can be fitted with a linear equation, as shown in Figure 3a and 3b, with a resulting goodness-of-fit (R^2) being 1.0, the two data sets for the optimized structures of site #1 and #2 in vacuum have been fitted with a second order polynomial expression each giving a goodness-of-fit of 1.0. While it would be interesting to use the fitting equations for optimized interfacial structures to determine by extrapolation the electric field strength at which all the surface potassium sites would be iso-energetic, care should be taken as the induced structural relaxations make the effects of electric fields on the relative energy deviate from a linear dependance. This is especially the case for the optimized orthoclase (001)/vacuum interface for which a second order polynomial expression has been used. While the fits obtained for structurally optimized orthoclase (001)/vacuum interface are good mathematical fits, it is unclear if they also provide a good physical and chemical description of the interface as electric fields induced structural relaxations can reach a breaking point where the surface ion desorbs (as discussed in the next section). Therefore, for both interfaces (i.e., orthoclase (001)/vacuum and orthoclase (001)/water) we propose to use the linearly fitted data set for unrelaxed relative

energy changes, which would provide an extrapolated upper limit of the electric field strength required to have iso-energetic surface sites. For the orthoclase (001)/vacuum interface, site #2 will be iso-energetic with site #1 for E=-0.61 eV/Å, and site #1 and site #2 will be iso-energetic with the crystallographic surface site when E=-4.45 eV/Å and -2.73 eV/Å, respectively. For the orthoclase (001)/water interface, site #2 will be iso-energetic with site #1 for E=-0.52 eV/Å, and site #1 and site #2 will be iso-energetic with the crystallographic surface site when E=-0.73 eV/Å and -0.62 eV/Å, respectively. While those extrapolated electric field strengths are large, it is interesting to note that the presence of water makes the surface potassium sites more sensitive to electric fields. This is indicated by the slope of the linear fits, which is larger in the case of the orthoclase (001)/water interface than for the orthoclase (001)/vacuum interface (Figure 3a and 3b).

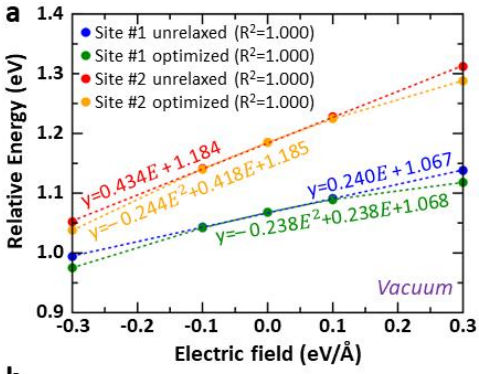
a
Site #1 unrelaxed (R²=1.000)
Site #1 optimized (R²=1.000)
Site #2 unrelaxed (R²=1.000)
Site #2 optimized (R²=1.000)
y=0.434E + 1.184
y=− 0.244E²+0.418E+1.185
y=0.240E + 1.067
y=− 0.238E²+0.238E+1.068
Vacuum
Relative Energy (eV)
Electric field (eV/Å)

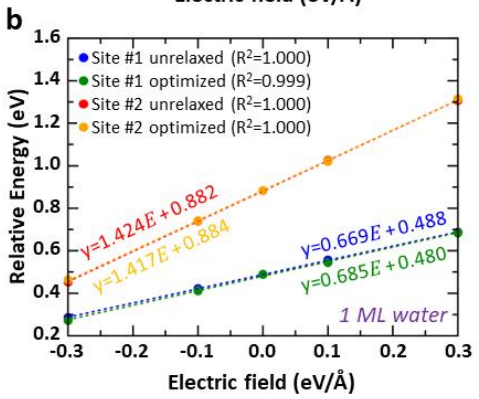
b
Site #1 unrelaxed (R²=1.000)
Site #1 optimized (R²=0.999)
Site #2 unrelaxed (R²=1.000)
Site #2 optimized (R²=1.000)
y=1.424E + 0.882
y=1.417E + 0.884
y=0.669E + 0.488
y=0.685E + 0.480
1 ML water
Relative Energy (eV)
Electric field (eV/Å)

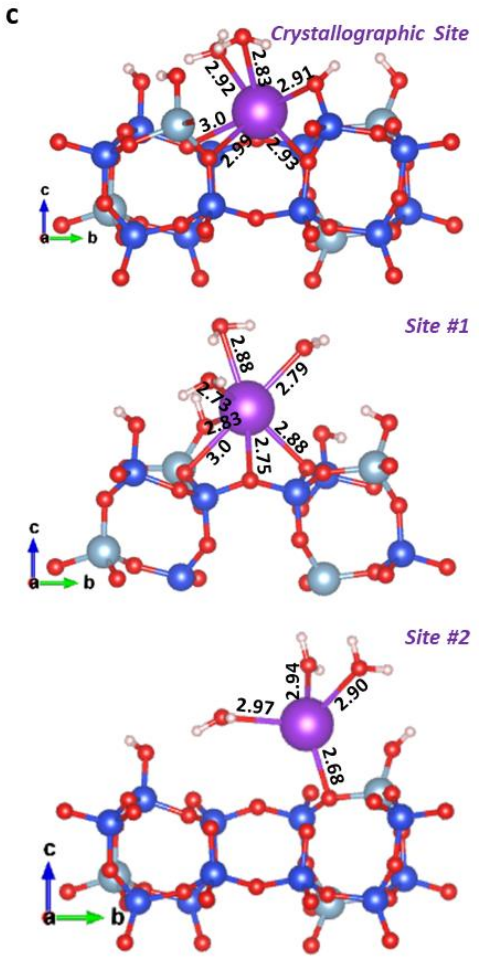
c
Crystallographic Site
Site #1
Site #2

Figure 3: Energy of two K^+ surface sites, labeled #1 and #2 in Figure 1c, relative to that of the crystallographic K^+ surface site as function of electric field intensity for the orthoclase (001) surface in (a) vacuum and (b) in contact with 1 ML of water. For each data set the fit is shown by a dashed line and the goodness-of-fit (R^2) is provided in the legend. (c) For the case where 1ML is present, at zero applied field, the coordination shell of the surface K^+ ions at the crystallographic site, site #1, and site #2 is shown, along with the K—O bond lengths (in Å). For sake of clarity, some surface atoms and too distant water molecules have been removed.

Effect of electric fields on the local structure of K^+ ions. To further understand the effects of electric fields on surface potassium binding, a bond length analysis was performed for potassium atoms located in sites #1 and #2 (Figure 4). For each calculated data set, a linear fit has been performed, as shown by the dashed lines, and the goodness-of-fit (R^2) is provided in the Figure legend. In Figure 4b, the value of R^2 for the average data is closer to zero (R^2=0.240) because the fit is essentially a constant value. At the orthoclase (001)/vacuum interface, the bond lengths between K^+ ions at both sites and nearby surface O atoms (labeled O_s) decrease for electric fields directed away from the surface (i.e., $E > 0$) and increase for electric fields directed toward the surface (i.e., $E < 0$), compared to the bond lengths obtained when no electric field is applied. This suggests that the direction and intensity of electric fields can be used to facilitate either adsorption or desorption of surface K^+ species. A similar but slightly more complex trend is predicted at the orthoclase (001)/water interface for sites #1 (Figure 4b) and #2 (Figure 4c). Those figures display the distances between K and O_s atoms and between K and water O atoms (labeled O_w) as well as the average K—O bond lengths. The average K—O distance is only slightly affected by the direction and intensity of the electric field at site #1 (Figure 4b) and site #2 (Figure 4c), however, this is the result of opposing trends in the dependence of K—O_s and K—O_w bond lengths on the electric field. While the K—O_s bond length follows a similar trend than previously described for the orthoclase (001)/vacuum interface, the K—O_w bond lengths follow the opposite trend, in which the hydration shell of surface K^+ atoms is more tightly bounded for electric fields directed toward the surface (i.e., $E < 0$) and is more loosely bounded for electric fields directed away from the surface (i.e., $E > 0$). The opposite trends obtained for K—O_s and K—O_w suggest that the direction and intensity of the electric field can facilitate either desorption or dehydration of surface K^+ ions. In the case of K^+ in site #2, the linear fit of the data in Figure 4c did not include the values at 0.3 eV/Å because they correspond to a change in the bonding pattern of surface K^+ which cannot be described by a linear fit. To help visualize the discontinuity, full lines have been plotted between 0.1 and 0.3 eV/Å, providing a guide to the eye, while the fitted data are represented by dashed lines. Figure 4c shows that a more abrupt increase of the distance between K and O_w is obtained for electric fields directed away from the surface and higher than 0.1 eV/Å. This could suggest the beginning of the loss of the hydration shell of surface K^+ cations

in favor of a stronger adsorption at this site. This also suggests that a potassium cation located in site #2 could more easily lose its hydration shell than a potassium cation located in site #1.

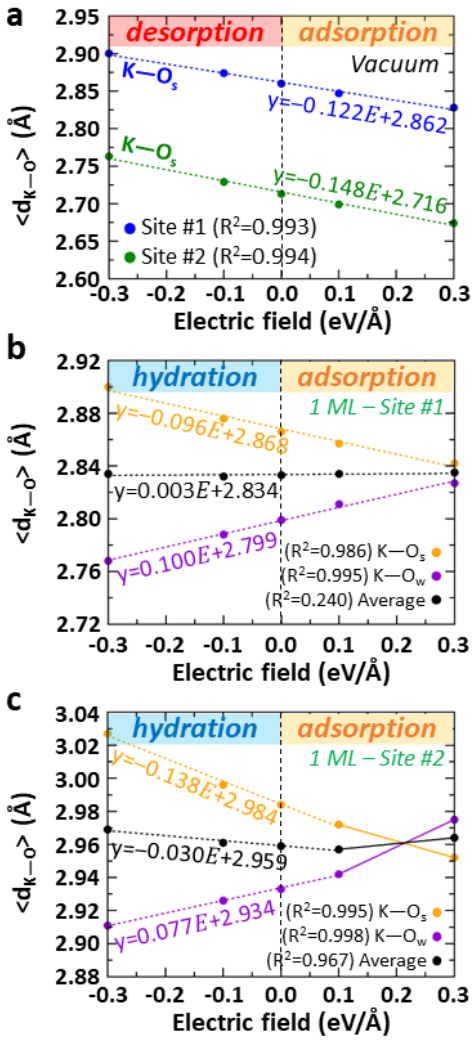

Figure 4: (a) Average distance ($<d_{K-O}>$) between surface K^+ at sites #1 and #2, and surface O, as function of electric field intensity for the orthoclase (001)/vacuum interface. (b) Average distance ($<d_{K-O}>$) between surface K^+ at site #1 and first neighbor surface and water oxygen atoms, respectively labeled O_s and O_w, at orthoclase (001)/water interface as function of electric field intensity. The black data represents the average of K—O_s and K—O_w bond lengths. (c) Similar bond length analysis than (b) reported for surface K^+ cation in site #2. For each data set the fit is shown by a dashed line and the goodness-of-fit (R^2) is provided in the legend.

Impact of electric fields on the migration energy barrier surface K^+ ions. All the electronic and structural changes described have an impact on the migration of surface K^+ cations to

neighboring sites. To quantify the effects of electric field intensity and direction on surface diffusion, CI-NEB calculations were performed to determine the migration energy barrier of surface K^+ ions from their crystallographic site, labeled K_c, to sites #1 and #2 respectively labeled $K_{\#1}$ and $K_{\#2}$ in Figure 5. A representation of the migration path to sites #1 and #2 is shown in Figures 5a and 5b, respectively. At both interfaces, the energy barrier for surface K^+ migration is reduced for an electric field directed toward the surface, while it is increased for an electric field directed away from the surface (Figures 5c and 5d). Combining these results with the changes obtained for the bond lengths indicates that an electric field directed toward the surface (i.e., $E < 0$) will favor desorption and facilitate surface migration, while an electric field directed away from the surface (i.e., $E > 0$) will favor sorption (or dehydration) and slow surface migration.

The result of a linear fit of the energy barriers obtained as function of the electric field intensity is also displayed for each case in Figure 5. The energy barrier variations induced by the electric field are smaller at the orthoclase (001)/vacuum interface than at the orthoclase (001)/water interface. This result indicates that the presence of water increases the sensitivity of surface K^+ migration to applied electric fields and facilitates the migration of surface K^+ cations because the energy barriers calculated at the orthoclase (001)/water interface are generally smaller than those obtained at the orthoclase (001)/vacuum interface.

It is interesting to estimate the electric field strength at which the surface migration of K^+ ions occur without energy barrier (i.e., 0 eV). Based on the linear fit obtained for each case (Figure 5), for path #1 and #2 at the orthoclase (001)/vacuum interface, the extrapolated electric field would be -3.28 eV/Å and -3.36 eV/Å respectively, and in the case of the orthoclase (001)/water interface, the extrapolated electric field strength would be -1.01 eV/Å and -0.74 eV/Å respectively. However, as shown earlier, electric fields directed toward the surface (i.e., $E < 0$) induce a desorption of surface K^+ (Figure 4) and, at these electric field strengths, the extrapolated bond length between K^+ and surface O atoms would increase to 3.26 Å and 3.22 Å for site #1 and #2 at the orthoclase (001)/vacuum interface, respectively. For site #1 and #2 at the orthoclase (001)/water interface, the K—O_s bond lengths would increase to 2.97 Å and 3.09 Å, respectively. While these bond lengths are longer than the sum of the covalent radius of each species (2.69 Å) but shorter than the sum of their van der Waals radius (4.23 Å), the strength of the electric field could play a role in the competition between surface K^+ migration and desorption.

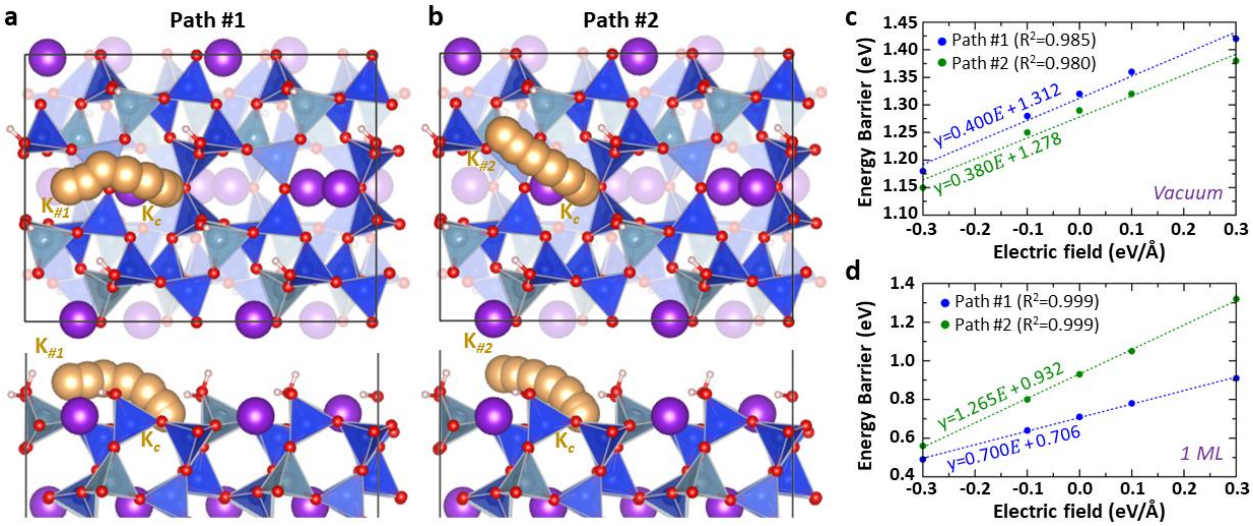

Figure 5: Representation of the two migration paths investigated for surface K^+ at the orthoclase (001) surface. (a) Top and side views of the migration path #1 from surface crystallographic site, labeled K_c, to surface site #1, labeled $K_{\#1}$. (b) Top and side views of the migration path #2 from surface crystallographic site, K_c, to surface site #2, labeled $K_{\#2}$. (c) Variations of the migration energy barrier for path #1 and #2 as function of electric field intensity for K^+ migration at orthoclase (001)/vacuum interface. (d) Variations of the migration energy barrier for path #1 and #2 as function of electric field intensity for K^+ migration at orthoclase (001)/water interface. For each data set the fit is shown by a dashed line and the goodness-of-fit (R^2) is provided in the legend.

Impact of electric fields on the residence time of surface K^+ ions. The calculated energy barriers, E_a, can be used to estimate the residence time, τ, of surface K^+ ions at their crystallographic sites. Using statistical thermodynamics, Vineyard[55] has shown that the jump rate, ω, which is the number of jumps per second, has an Arrhenius-type dependence on temperature and can be written as:

$$\omega = \nu_0 \mathrm{e}^{-\frac{E_a}{k_\mathrm{B}T}}, \quad (1)$$

where ν_0, k_B, and T are respectively the attempt frequency, which is typically of the order of the Debye frequency, ranging from 10^{12} to 10^{13} s^{-1} for practically all solids,[56] the Boltzmann constant (in $eV.K^{-1}$), and the temperature (in K). By fixing ν_0 to 10^{13} s^{-1}, the residence time (in s) has been calculated as $\tau = \frac{1}{\omega}$ and shown in Figure 6. The calculated residence times for the orthoclase (001)/vacuum and orthoclase (001)/water interfaces have been fitted with an exponential equation which yielded a goodness-of-fit close to 1. Figure 6 clearly shows that the residence time at the orthoclase (001)/water interface is more affected by electric fields than at the orthoclase (001)/vacuum interface. For electric fields directed toward the surface (i.e., $E < 0$),

desorption is favored leading to shorter residence time of surface K^+ ion at its crystallographic site, while for electric fields directed away from the surface (i.e., $E > 0$), sorption (or dehydration) is favored which leads to longer residence time of surface K^+ ion in its crystallographic site. Depending on the strength of the electric field applied, the residence time can be affected by several orders of magnitude. However, in the case where the electric field strength is comparable to the Earth's electric field (~100 V/m), the changes in the residence time would be extremely small, about 7 orders of magnitude less (i.e., a tenth of microsecond) than the calculated residence time. That is, for a residence time in the order of 0.1 s (i.e., path #1 – 1 ML at an electric field of 0 eV/Å), the changes in residence time would be in the order of 10^{-8} s at Earth's electric field.

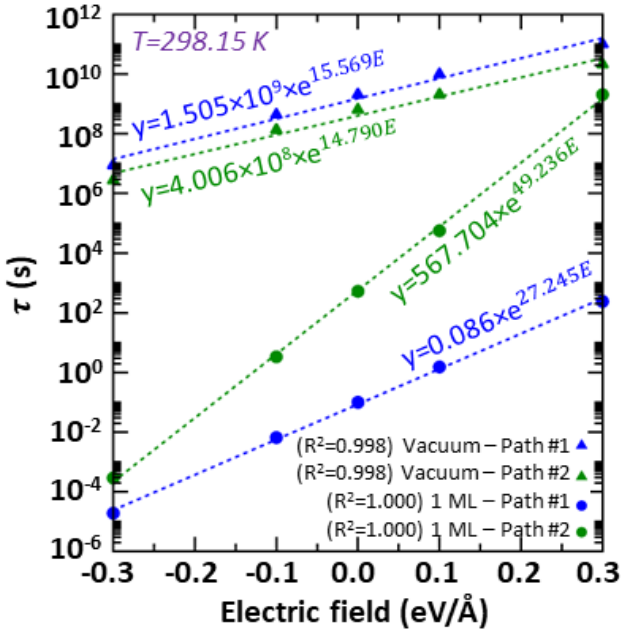

Figure 6: Calculated residence time, τ, of surface K^+ ions in their crystallographic sites as function of electric field intensity at 298.15 K. The residence time calculated for each path at the orthoclase (001)/vacuum and orthoclase (001)/water interfaces are shown by triangles and circles, respectively. For each data set the fit is shown by a dashed line and the goodness-of-fit (R^2) is provided in the legend.

Conclusions

Density functional theory calculations were performed to quantify the effects of applied electric fields on the electronic structure of and migration of surface K^+ cations at orthoclase (001)/vacuum and orthoclase (001)/water interfaces. Electric fields were found to induce a polarization of the electronic cloud of the surface atoms without causing noticeable charge

transfer. When a monolayer of water is present, K^+ cations are forming partially hydrated inner-sphere complexes at the interface. For potassium in site #2, a monodentate contact with the surface and a hydration shell less tightly bound to surface K^+ is obtained compared to potassium in site #1. The presence of a monolayer of water facilitates surface K^+ migration while increasing the response of different surface potassium sites to applied electric fields. The calculations also showed that the direction of the electric field affects the residence time and sorption behavior of surface K^+ cations. While electric fields directed toward the surface facilitate surface K^+ migration by favoring desorption, electric fields directed away from the surface slows surface K^+ migration by favoring sorption and dehydration. The response of the interfaces to electric fields can impact the residence time of K^+ ions at the crystallographic site by several orders of magnitude, depending on the strength of the field and extent of hydration.

This work represents a first step using DFT to address field-driven ion dynamics in the Stern layer of the EDL at common mineral surfaces. There are many important directions for future work along these lines. The dependence of the field effects on surface orientation is a potentially important open question. Further surface structural experimental investigations at single crystal orthoclase surfaces, particularly under applied electric fields, would ideally complement our understanding of EDL behavior under applied electric fields. Column-scale EIS/SIP measurements on homogeneous mono-mineralic porous media under controlled conditions of pore saturation or fixed relative humidities would also provide a useful target for atomic-to-mesoscale simulations of the polarization response. Combined work of this nature could ultimately provide a basis for development of improved EDL models that encompass the dynamics of ion-ion and ion-surface interactions.

Author Information:

Corresponding Author

*E-mail: michel.sassi@pnnl.gov

ORCID:

Michel Sassi: 0000-0003-2582-3735

Sebastien N. Kerisit: 0000-0002-7470-9181

Pauline G. Simonnin: 0000-0002-6197-7435

Benjamin A. Legg: 0000-0002-3055-1829

Elias Nakouzi: 0000-0003-0036-8326

Yue Zhu: 0000-0001-6626-2263

Timothy C. Johnson: 0000-0001-9514-6288

Kevin M. Rosso: 0000-0002-8474-7720

Acknowledgements:

This research was supported by the Laboratory Directed Research and Development (LDRD), Induced Spectral Imaging Technology for the Environment (INSITE) project at Pacific Northwest National Laboratory (PNNL). PNNL is a multi-program national laboratory operated for the DOE by Battelle Memorial Institute under Contract No. DE-AC05-76RL01830. Computational resources were provided by PNNL Institutional Computing (PIC).

Author contributions:

All authors interpreted the results, drafted, reviewed, and revised the manuscript.

Associated Content:

The atomic coordinates of the hydrated slab model are provided in supplementary information.

Competing interests:

The authors declare no competing financial interest.

References:

1. Henderson, D.; Boda, D. Insights from Theory and Simulation on the Electrical Double Layer. *Phys. Chem. Chem. Phys.* **2009**, *11*, 3822-3830.
2. Bourg, I. C.; Lee, S. S.; Fenter, P.; Tournassat, C. Stern Layer Structure and Energetics at Mica-Water Interfaces. *J. Phys. Chem. C* **2017**, *121*, 9402-9412.
3. Brown Jr., G. E.; Henrich, V. E.; Casey, W. H.; Clark, D. L.; Eggleston, C.; Felmy, A.; Goodman, D. W.; Grätzel, M.; Maciel, G.; McCarth, M. I. *et al.* Metal Oxide Surfaces and Their Interactions with Aqueous Solutions and Microbial Organisms. *Chem. Rev.* **1999**, *99*, 77-174.
4. Wu, J. Understanding the Electric Double-Layer Structure, Capacitance, and Charging Dynamics. *Chem. Rev.* **2022**, *122*, 10821-10859.
5. Banuelos, J.; Borguet, E.; Brown, G.; Cygan, R.; De Yoreo, J.; Dove, P.; Gaigeot, M.-P.; Geiger, F.; Gibbs, J.; Grassian, V. et al. Oxide- and Silicate-Water Interfaces and Their Roles in Technology and the Environment. *Chem. Rev.* **2023**, *123*, 6413-6544.
6. Ding, Z.; Kloprogge, J. T.; Frost, R. L.; Lu, G. Q.; Zhu, H. Y. Porous Clays and Pillared Clays-Based Catalysts. Part 2: A Review of the Catalytic and Molecular Sieve Applications. *J. Porous Mater.* **2002**, *8*, 273-293.
7. Arnold, J.; Kosson, D. S. S.; Garrabrants, A.; Meeussen, J. C. L. C. L.; van der Sloot, H. A. A. Solution of the Nonlinear Poisson−Boltzmann Equation: Application to Ionic Diffusion in Cementitious Materials. *Cem. Concr. Res.* **2013**, *44*, 8-17.
8. Brown, G. E., Jr. How Minerals React with Water. *Science* **2001**, *294*, 67-69.
9. Zachara, J.; Brantley, S.; Chorover, J.; Ewing, R.; Kerisit, S.; Liu, C.; Perfect, E.; Rother, G.; Stack, A. G. Internal Domains of Natural Porous Media Revealed: Critical Locations for Transport, Storage, and Chemical Reaction. *Environ. Sci. Technol.* **2016**, *50*, 2811-2829.
10. Liu, L. Prediction of Swelling Pressures of Different Types of Bentonite in Dilute Solutions. *Colloids Surf. A* **2013**, *434*, 303-318.
11. Tinnacher, R. M.; Holmboe, M.; Tournassat, C.; Bourg, I. C.; Davis, J. A. Ion Adsorption and Diffusion in Smectite: Molecular, Pore, and Continuum Scale Views. *Geochim. Cosmochim. Acta* **2016**, *177*, 130-149.
12. Lyklema, J; Dukhin, S.S.; Shilov, V.N. The relaxation of the double layer around colloidal particles and the low-frequency dielectric dispersion: Part I. Theoretical considerations. *J. Electroanal. Chem.* **1983**, *143*, 1-21.
13. Placencia-Gómez, E.; Parviainen, A.; Slater, L.; Leveinen, J.; Spectral induced polarization (SIP) response of mine tailings. *J. Contam. Hydrol.* **2015**, *173*, 8-24.
14. Binley, A.; Slater, L. D.; Fukes, M.; Cassiani, G. Relationship between spectral induced polarization and hydraulic properties of saturated and unsaturated sandstone. *Water Resour. Res.* **2005**, *41*, W12417.
15. Kemna, A.; Binley, A.; Cassiani, G.; Niederleithinger, E.; Revil, A.; Slater, L.; Williams, K. H.; Orozco, A. F.; Haegel, F. H.; Hordt, A.; Kruschwitz, S.; Leroux, V.; Titov, K.; Zimmermann, E.

An overview of the spectral induced polarization method for near-surface applications. *Near Surf. Geophys.* **2012**, *10*, 453-468.

16. Atekwana, E. A.; Slater, L. D. Biogeophysics: A New Frontier in Earth Science Research. *Rev. Geophys.* **2009**, *47*, RG4004.
17. Wu, Y.; Slater, L. D.; Korte, N. Effect of Precipitation on Low Frequency Electrical Properties of Zerovalent Iron Columns. *Environ. Sci. Technol.* **2005**, *39*, 9197-9204.
18. Slater, L.; Ntarlagiannis, D.; Wishart D. On the relationship between induced polarization and surface area in metal-sand and clay-sand mixtures. *Geophysics* **2006**, *71*, A1-A5.
19. Joseph, S.; Aluru, N. R. Hierarchical Multiscale Simulation of Electrokinetic Transport in Silica Nanochannels at the Point of Zero Charge. *Langmuir* **2006**, *22*, 9041-9051.
20. Biriukov, D.; Fibich, P.; Předota, M. Zeta Potential Determination from Molecular Simulations. *J. Phys. Chem. C* **2020**, *124*, 3159-3170.
21. Botan, A.; Rotenberg, B.; Marry, V.; Turq, P.; Noetinger, B. Hydrodynamics in Clay Nanopores. *J. Phys. Chem. C* **2011**, *115*, 16109-16115.
22. Plümper, O.; Botan, A.; Los, C.; Liu, Y.; Malthe-Sørenssen, A.; Jamtveit, B. Fluid-Driven Metamorphism of the Continental Crust Governed by Nanoscale Fluid Flow. *Nature Geosci.* **2017**, *10*, 685-691.
23. Kerisit, S.N.; Simonnin, P.G.; Sassi, M.; Rosso, K.M. Electric field effects on water and ion structure and diffusion at the orthoclase (001)-water interface. *J. Phys. Chem. C* **2023**, *127*, 7389-7401.
24. Xu, R.; Zou, X. Electric Field-Modulated Magnetic Phase Transition in van der Waals CrI_3 Bilayers. *J. Phys. Chem. Lett.* **2020**, *11*, 3152-3158.
25. Che, F.; Gray, J. T.; Ha, S.; McEwen, J.-S. Catalytic Water Dehydrogenation and Formation on Nickel: Dual Path Mechanism in High Electric Fields. *J. Catal.* **2015**, *332*, 187-200.
26. Feibelman, P. J. Surface-diffusion Mechanism versus Electric Field: Pt/Pt(001). *Phys. Rev. B* **2001**, *64*, 125403.
27. Harrison, R. G. Fair weather atmospheric electricity. *J. Phys.: Conf. Ser.* **2011**, *301*, 012001.
28. Velpula, G.; Teyssandier, J.; De Feyter, S.; Mali, K.S. Nanoscale Control over the Mixing Behavior of Surface-Confined Bicomponent Supramolecular Networks Using an Oriented External Electric Field. *ACS Nano* **2017**, 11, 10903-10913.
29. Hu, H.; Dai, L.; Li, H.; Jiang, J.; Hui, K. Electrical conductivity of K-feldspar at high temperature and high pressure. *Miner. Petrol.* **2014**, *108*, 609-618.
30. Hiranuma, N.; Möhler, O.; Yamashita, K.; Tajiri, T.; Saito, A.; Kiselev, A.; Hoffmann, N.; Hoose, C.; Jantsch, E.; Koop, T.; Murakami, M. Ice nucleation by cellulose and its potential contribution to ice formation in clouds. *Nature Geosci.* **2015**, *8*, 273-277.

31. Wilson, T.; Ladino, L.; Alpert, P.; Breckels, M. N.; Brooks, I. M.; Browse, J.; Burrows, S. M.; Carslaw, K. S.; Huffman, J. A.; Judd, C. *et al.* A marine biogenic source of atmospheric ice-nucleating particles. *Nature* **2015**, *525*, 234-238.

32. Atkinson, J.; Murray, B.; Woodhouse, M.; Whale, T. F.; Baustian, K. J.; Carslaw, K. S.; Dobbie, S.; O'Sullivan, D.; Malkin, T. L. The importance of feldspar for ice nucleation by mineral dust in mixed-phase clouds. *Nature* **2013**, *498*, 355-358.

33. Kiselev, A.; Bachmann, F.; Pedevilla, P.; Cox, S. J.; Michaelides, A.; Gerthsen, D.; Leisner, T. Active sites in heterogeneous ice nucleation - the example of K-rich feldspars. *Science* **2017**, *355*, 367-371.

34. Zolles, T.; Burkart, J.; Häusler, T.; Pummer, B.; Hitzenberger, R.; Grothe, H. Identification of Ice Nucleation Active Sites on Feldspar Dust Particles. *J. Phys. Chem. A* **2015**, *119*, 2692-2700.

35. Kresse, G.; Furthmuller, J. Efficient Iterative Schemes for Ab Initio Total-Energy Calculations Using a Plane-Wave Basis Set. *Physical Review B* **1996**, *54*, 11169-11186.

36. Kresse, G.; Furthmuller, J. Efficiency of Ab-Initio Total Energy Calculations for Metals and Semiconductors Using a Plane-Wave Basis Set. *Comput. Mater. Sci.* **1996**, *6*, 15-50.

37. Kresse, G.; Hafner, J. Ab Initio Molecular Dynamics for Liquid Metals. *Phys. Rev. B* **1993**, *47*, 558-561.

38. Kresse, G.; Hafner, J. Ab Initio Molecular-Dynamics Simulation of the Liquid-Metal-Amorphous-Semiconductor Transition in Germanium. *Phys. Rev. B* **1994**, *49*, 14251-14269.

39. Perdew, J. P.; Burke, K.; Ernzerhof, M. Generalized Gradient Approximation Made Simple. *Physical Review Letters* **1996**, *77*, 3865-3868.

40. Grimme, S.; Antony, J.; Ehrlich, S.; Krieg, H. A Consistent and Accurate Ab Initio Parametrization of Density Functional Dispersion Correction (DFT-D) for the 94 Elements H-Pu. *Journal of Chemical Physics* **2010**, *132*, 154104.

41. Kimata, M.; Saito, S.; Shimizu, M.; Iida, I.; Matsui, T. Low temperature crystal structures of Orthoclase and Sanidine. *N. Jb. Miner. Abh.* **1996**, *171*, 199-213.

42. Kerisit, S.; Liu, C.; Ilton, E. S. Molecular Dynamics Simulations of the Orthoclase (001)- and (010)-Water Interfaces. *Geochim. Cosmochim. Acta* **2008**, *72*, 1481-1497.

43. Kerisit, S. and Liu, C. Molecular Simulations of Water and Ion Diffusion in Nanosized Mineral Fractures. *Environ. Sci. Technol.* **2009**, *43*, 777-782.

44. Kerisit, S.; Liu, C. Diffusion and Adsorption of Uranyl Carbonate Species in Nanosized Mineral Fractures. *Environ. Sci. Technol.* **2012**, *46*, 1632-1640.

45. Kerisit, S.; Liu, C. Molecular Dynamics Simulations of Uranyl and Uranyl Carbonate Adsorption at Aluminosilicate Surfaces. *Environ. Sci. Technol.* **2014**, *48*, 3899-3907.

46. Monkhorst, H. J.; Pack, J. D. Special points for Brillouin-zone integrations. *Phys. Rev. B* **1976**, *13*, 5188.

47. Yeh, C.-H.; Le Pham, T. M.; Nachimuthu, S.; Jiang, J.-C. Effect of External Electric Field on Methane Conversion on IrO2(110) Surface: A Density Functional Theory Study. *ACS Catal.* **2019**, *9*, 8230-8242.

48. Neugebauer, J.; Scheffler, M. Adsorbate-Substrate and Adsorbate-Adsorbate Interactions of Na and K Adlayers on Al(111). *Phys. Rev. B* **1992**, *46*, 16067-16080.

49. Henkelman, G.; Jónsson, H. A climbing image nudged elastic band method for finding saddle points and minimum energy paths. *J. Chem. Phys.* **2000**, *113*, 9901-9904.

50. Tang, W.; Sanville, E.; Henkelman, G. A grid-based Bader analysis algorithm without lattice bias. *J. Phys.: Condens. Matter* **2009**, *21*, 084204.

51. Sanville, E.; Kenny, S. D.; Smith, R.; Henkelman, G. An improved grid-based algorithm for Bader charge allocation. *J. Comp. Chem.* **2007**, *28*, 899-908.

52. Henkelman, G.; Arnaldsson, A.; Jónsson, H. A fast and robust algorithm for Bader decomposition of charge density. *Comput. Mater. Sci.* **2006**, *36*, 354-360.

53. Yu, M.; Trinkle, D. R. Accurate and efficient algorithm for Bader charge integration. *J. Chem. Phys.* **2011**, *134*, 064111.

54. https://theory.cm.utexas.edu/vtsttools/index.html (accessed on February 2nd, 2023).

55. Vineyard, G. H. Frequency factors and isotropy effects in solid state rate processes. *J. Phys. Chem. Solids* **1957**, *3*, 121-127.

56. Mehrer, H. Diffusion in solids: Fundamentals, methods, materials, diffusion-controlled processes. *Springer Series in Solid State Science*. 155, **2007**.

Graphic Abstract: